PAPER • OPEN ACCESS

Geometry effects in topologically confined bilayer graphene loops

New Journal of Physics
The open access journal at the forefront of physics

Deutsche Physikalische Gesellschaft DPG
IOP Institute of Physics

Published in partnership with: Deutsche Physikalische Gesellschaft and the Institute of Physics

OPEN ACCESS

RECEIVED
15 October 2021

REVISED
13 December 2021

ACCEPTED FOR PUBLICATION
15 December 2021

PUBLISHED
30 December 2021

PAPER

Geometry effects in topologically confined bilayer graphene loops

Nassima Benchtaber[1], **David Sánchez**[1,2] and **Llorenç Serra**[1,2,*]

[1] Institute for Cross-Disciplinary Physics and Complex Systems IFISC (CSIC-UIB), E-07122 Palma, Spain
[2] Department of Physics, University of the Balearic Islands, E-07122 Palma, Spain
[*] Author to whom any correspondence should be addressed.

E-mail: llorens.serra@uib.es

Keywords: bilayer graphene, topological states, persistent currents, quantum nanostructures

Abstract

We investigate the electronic confinement in bilayer graphene by topological loops of different shapes. These loops are created by lateral gates acting via gap inversion on the two graphene sheets. For large-area loops the spectrum is well described by a quantization rule depending only on the loop perimeter. For small sizes, the spectrum depends on the loop shape. We find that zero-energy states exhibit a characteristic pattern that strongly depends on the spatial symmetry. We show this by considering loops of higher to lower symmetry (circle, square, rectangle and irregular polygon). Interestingly, magnetic field causes valley splittings of the states, an asymmetry between energy reversal states, flux periodicities and the emergence of persistent currents.

1. Introduction

One of the most fundamental predictions of Quantum Mechanics is the existence of confined or bound states which are eigenstates of the Hamiltonian describing a particular system [1]. It is well known that the Schrödinger equation with a spatially dependent potential yields in many cases bound eigenstates located around the absolute potential minima. This potential binding mechanism around minima is crucial in many natural physical systems like, e.g. electrons in atoms and molecules [2]; and it is also behind the formation of artificial bound states by potential gating with microelectrodes, as in semiconductor quantum dots [3]. In bilayer graphene (BLG) with Bernal stacking, the material we consider in this work, a similar potential confinement mechanism exists but it is related to the potential difference V_a applied to split dual gates on the two graphene sheets; electrons are bound to the regions where V_a is lowest. These regions of lowest V_a can take different shapes, such as circular dots and rings for instance, and they have been intensively studied both theoretically and experimentally [4–17]. The technological interest of BLG nanostructures is twofold. First, they could serve as scalable spin qubits with long decoherence times due to the weak spin–orbit interaction in graphene [18–20]. Second, in combination with magnetic fields they could be utilized for valleytronic operations thanks to the manipulation of the valley degree of freedom [21–23].

The possibility of an even more robust type of confinement in BLG was suggested in reference [24]. This is a qualitatively different confinement, of a topological character, emerging near the domain wall that separates two regions where V_a changes sign. The confined states are intrinsically 1D-like, with a characteristic transverse decay length, and they propagate along the domain wall with locked relative orientations of momentum and valley pseudospin. In the absence of valley mixing potentials states for the K and K′ valleys propagate along the wall, without backscattering, showing opposite chiralities. This property is similar to the helical states within the quantum spin Hall effect [25–27] if we replace spin with the valley pseudospin of graphene.

Now, let us suppose that the external gates are arranged in such a way that the domain wall closes into itself. A schematic representation is shown in figure 1(a). Then, a loop forms supporting electronic bound states [28] and the following question naturally arises. What is the effect of different loop shapes onto the

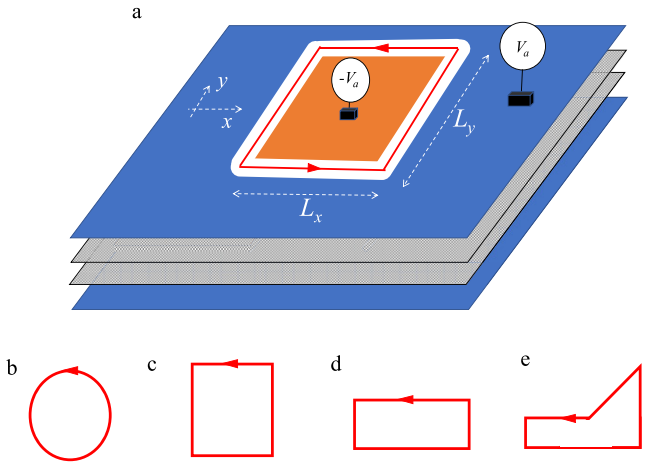

Figure 1. (a) Scheme of a topological loop showing the BLG sheets (gray) and lateral gates with the applied gate potentials $\pm V_a$ (orange and blue, respectively). Two identical lower gates, hidden behind the lower graphene sheet, have the opposite potentials of the corresponding top gates. The white 1D region between orange and blue gates hosts the topological loop state on the graphene sheets, with counterpropagation for the two valleys. A red arrow is indicating the circulation for only one of the two valleys. (b)–(e) Loop shapes considered in this work, from highest to lowest symmetry: circle, square, rectangle and irregular polygon.

energy spectrum of these bound states? Being 1D-like, topologically confined sates in BLG are expected to essentially depend on the loop perimeter unlike the trivial potential confinement, which depends both on the surface and the shape of the confining region. Nevertheless, it is important to notice that the domain-wall states depicted with a red line in figure 1(a) are in reality quasi-1D with a finite spatial width. Therefore, the discrete energy spectrum will be in general a function of the system's geometrical symmetries, the region aspect ratio, etc. Below, we present a detailed investigation for topological loops of different shapes and symmetries. First, we show with the aid of an exactly solvable model that the energy spectrum is uniquely determined by the loop perimeter provided that the system size is large. Yet, for smaller loops finite size effects become important and the spectrum depends on the particular geometrical structure. This dependence is better seen in the sequence of zero energy crossing and anticrossings as the perimeter increases.

In presence of a magnetic field B, the dispersion is affected by the flux piercing the topological loop. This creates an energy splitting for the two valleys and an asymmetry with respect to energy inversion ($E \to -E$) in the spectra as a function of perimeter. The B-dependence of the spectra with a fixed perimeter and shape is characterized by magnetic periodicities of Aharonov–Bohm type. Therefore, the loops host persistent currents at finite fields that, similarly to the $B = 0$ spectra, exhibit geometry dependent features in the small size limit, showing that currents would serve as an excellent tool to probe topologically confined states in BLG nanostructures.

2. Theory

2.1. A quantum perimeter model (QPM)

An analytic model of topological loops in BLG can be devised utilizing the results of reference [24] for a straight domain wall with an abrupt transition $+V_a$ to $-V_a$ (a kink). The analytic relations between linear momentum p along the kink and energy E of the two topological branches, corresponding to the two valleys (K, K'), were given in reference [24] as $p = f_{1,2}(E)$, with

$$f_{1,2}(E) = \frac{-E \pm \frac{V_a}{\sqrt{2}}}{\left(\mp E + V_a\sqrt{2}\right)^{1/2}} \frac{\sqrt{t}}{v_F}, \tag{1}$$

where the Fermi velocity $\hbar v_F = 660$ meV nm and the interlayer coupling $t = 380$ meV are BLG intrinsic parameters.

In a closed loop of perimeter $\mathcal{P}$ we can assume that the tangent momentum p is quantized, such that an integer number of wavelengths must fit into $\mathcal{P}$,

$$p \to p_n \equiv \hbar \frac{2\pi n}{\mathcal{P}}, \quad n = \pm 1, \pm 2, \ldots, \tag{2}$$

where negative n's represent negative momenta (i.e. opposite propagation) and the perimeter quantization in terms of wavelength λ reads $\mathcal{P} = |n|\lambda$. Since the Berry phase in BLG is 2π [29], its effect is already contained in the integer n's of equation (2) (see appendix A for an explicit check). We can also add a magnetic field, represented by a vector potential $\vec{A}$, and write the circulation integral

$$\int_{\mathcal{P}} \mathrm{d}l \left(p_n + eA_\mathrm{t}\right) = f_{1,2}(E) \int_{\mathcal{P}} \mathrm{d}l, \tag{3}$$

where A_t is the component of the vector potential tangent to the kink. Noticing that $\int_{\mathcal{P}} \mathrm{d}l = \mathcal{P}$ and $\int_{\mathcal{P}} A_\mathrm{t}\, \mathrm{d}l = SB \equiv \Phi$ (S, B and Φ being the loop surface, the perpendicular magnetic field and the magnetic flux, respectively) we find an implicit condition from which one can derive the bound state energy E for a given loop perimeter, magnetic flux and principal quantum number n:

$$f_{1,2}(E) = \frac{2\pi\hbar}{\mathcal{P}} \left(\frac{\Phi}{\Phi_0} + n\right), \tag{4}$$

where $\Phi_0 = h/e$ is the flux quantum.

Equation (4) is our QPM for bound states in BLG topological loops. As anticipated, when $\Phi = 0$ the relation depends only on the perimeter and is totally independent of the loop geometry. At finite fields, however, the bound-state energies depend on the loop surface through the Aharonov–Bohm flux ratio Φ/Φ_0. We expect the QPM to be reliable for large enough loops, when different parts of the loop do not interfere. In small loops, the traversal extension of the topological states becomes comparable to the distances inside the loop and the QPM breaks down. Below, we investigate deviations from the QPM using an exact approach for BLG within the continuum limit.

2.2. A quantum 2D model (Q2DM)

The low-energy Hamiltonian describing the states that are formed in two-dimensional (2D) BLG nanostructures for energies near the Dirac points reads [30, 31]

$$H = v_\mathrm{F} \left(p_x - \hbar \frac{y}{2l_z^2}\right) \tau_z \sigma_x + v_\mathrm{F} \left(p_y + \hbar \frac{x}{2l_z^2}\right) \sigma_y + \frac{t}{2} \left(\lambda_x \sigma_x + \lambda_y \sigma_y\right) + V_\mathrm{a}(x,y)\lambda_z, \tag{5}$$

where $\sigma_{x,y,z}$, $\tau_{x,y,z}$ and $\lambda_{x,y,z}$ are Pauli matrices for the sublattice, valley and layer pseudo spins, respectively. A topological loop forms from a space dependent function $V_\mathrm{a}(x,y)$ that, as sketched in figure 1(a), takes the constant values $+V_\mathrm{a}$ $(-V_\mathrm{a})$ outside (inside) the loop. In our numerical simulations, we consider a smooth spatial transition with a diffusivity [32] $s = 12.5$ nm to mimic a realistic experiment [33, 34]. Details of how we model the closed loops of different shapes are given in appendix A. Finally, the perpendicular field strength B is included in the magnetic length $l_z = \sqrt{\hbar/eB}$.

We numerically look for the eigenstates of the Hamiltonian given by equation (5) using finite difference discretization of the xy plane in a square grid [35]. The spurious solutions due to Fermion doubling [36–38] have been filtered out as in reference [32] by coarse graining the wave functions. Our method can handle any symmetry of the loop, in contrast to radial grids which are of smaller dimension and more efficient computationally, but can only describe radially symmetric structures by construction [7]. In all the cases treated below we have checked that good convergence with the grid size is reached.

The Hamiltonian equation (5) fulfills a chiral symmetry given by operator $\mathcal{C} = \sigma_x \tau_x \lambda_y$ relating eigenstates of opposite energies $\mathcal{C}^{-1} H \mathcal{C} = -H$ with $\mathcal{C}^2 = 1$ and $\mathcal{C}^{-1} = \mathcal{C}$. In absence of magnetic field it also fulfills time reversal symmetry $\Theta = i\tau_y \mathcal{K}$, with $\mathcal{K}$ representing complex conjugation, giving $\Theta^{-1} H \Theta = H$ with $\Theta^2 = -1$ and $\Theta^{-1} = -\Theta$. Notice that the presence of valley pseudospin yields $\Theta^2 = -1$, which is similar to the result for time reversal inversion of a spin 1/2 system. Differently to $\mathcal{C}$-symmetry, the result $\Theta^{-1} H \Theta = H$ implies a relation between states of the same energy. That is, if $|a\rangle$ is an energy eigenstate, then $\Theta|a\rangle$ and $\mathcal{C}|a\rangle$ are energy eigenstates of the same and opposite energies, respectively. We stress that both $\mathcal{C}$ and Θ are valley flip symmetry transformations due to the $\tau_{x,y}$ Pauli matrices.

3. Results

Figure 2 compares the bound state energies in the analytical (QPM) and numerical (Q2DM) approaches as a function of the loop perimeter when the structure is a circle. Qualitatively, both approaches nicely agree. At zero energy and zero field, equation (4) from the QPM predicts a sequence of uniformly spaced branch crossings, with spacing given by the zero-energy wavelength

$$\lambda_0 = 2^{3/4} \frac{2\pi\hbar v_\mathrm{F}}{\sqrt{V_\mathrm{a} t}}, \tag{6}$$

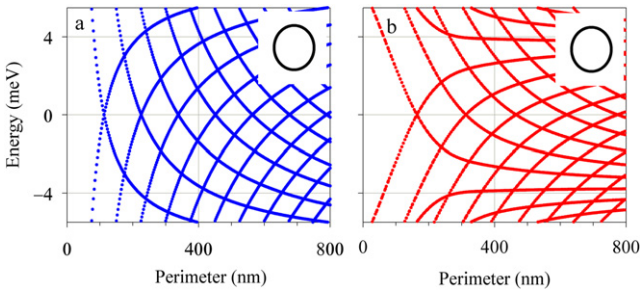

Figure 2. QPM (a) and Q2DM (b) energy spectrum for a circle as a function of its perimeter at zero magnetic field. Parameters: wall potential $V_a = 10$ meV and smoothness $s = 12.5$ nm.

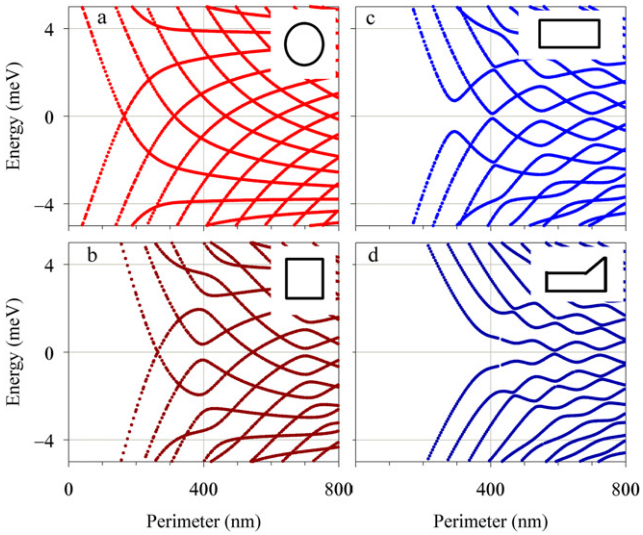

Figure 3. Q2DM energy spectra as a function of perimeter for circle (a), square (b), rectangle with aspect ratio $L_y = L_x/2$ (c) and irregular polygon (d). Parameters as in figure 2.

which for $V_a = 10$ meV yields $\lambda_0 \simeq 113$ nm. We then find a qualitatively good correspondence with the zero energy crossings obtained numerically in the Q2DM. Physically, in a ring each branch corresponds to an angular momentum $L_z \equiv xp_y - yp_x$ and, therefore, can produce crossings with additional branches of different angular momenta. For energies departing from zero, the main difference between panels (a) and (b) of figure 2 is that the energy branches are more densely spaced in Q2DM than QPM. This difference can be attributed to the small diffusivity $s = 12.5$ nm used in the QD2M. A smoother 1D kink is known to reduce the spacing of energy branches [32, 39].

In figure 3 we show the Q2DM energy spectra for different loop shapes as a function of their perimeters. Remarkably, the spectrum for noncircular loops show anticrossings of the branches. The square (b) shows an alternation of zero energy crossings and anticrossings as the perimeter increases. Both the rectangle (c) and the irregular polygon (d) show zero energy anticrossings in all cases, although the size of the anticrossing gap is not uniform. There is a general tendency for all shapes to decrease the anticrossing gaps for large perimeter, making the spectra shape independent in this limit.

The fact that, in addition to the circle, only the square shows crossings for some branches can be understood as a symmetry consequence. Inspired by the QPM, the branch crossing is possible in a square when, simultaneously, two conditions are fulfilled

$$\begin{cases} \mathcal{P} = n_1\lambda_0, \\ e^{ik_0L_x} = \pm i \Rightarrow \mathcal{P} = (2n_2+1)\lambda_0, \end{cases} \qquad n_1, n_2 \in \mathbb{N}, \tag{7}$$

where $k_0 = 2\pi/\lambda_0$ is the mode wavenumber. Only with n_1 odd the crossing is then possible, as indeed obtained in figure 3(b). The second condition in equation (7) corresponds to the requirement that a translation along the perimeter by the length of a side changes the state in a $\pm i$ phase, which occurs when the total number of wavelengths to distribute in the four square sides is odd $n_1 = 2n_2 + 1$. In a rectangle

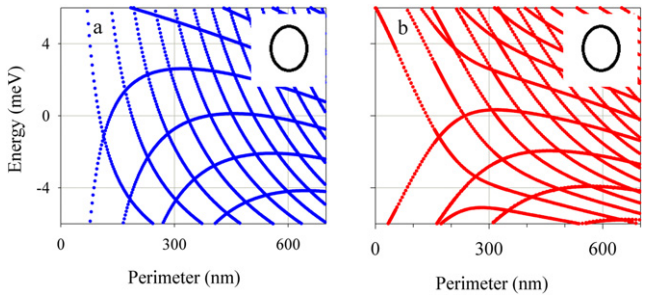

Figure 4. Same as figure 2 with a finite magnetic field. Parameters: wall potential $V_a = 10$ meV, smoothness $s = 12.5$ nm and magnetic field $B = 0.5$ T.

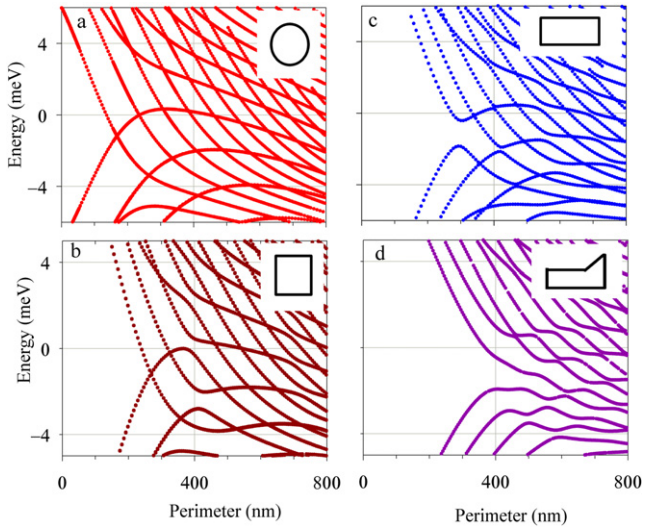

Figure 5. Same as figure 3 with a finite magnetic field $B = 0.5$ T. Parameters as in figure 4.

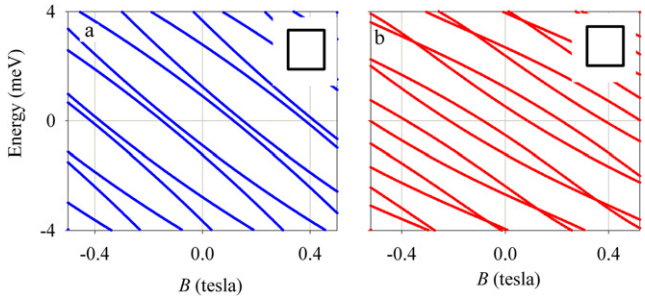

Figure 6. Spectrum as a function of magnetic field for a square loop of a fixed perimeter in QPM (a) and Q2DM (b). Parameters: wall potential $V_a = 10$ meV, smoothness $s = 12.5$ nm and perimeter $\mathcal{P} = 500$ nm.

one should replace L_x by $L_x + L_y$ in this second condition, which then becomes incompatible with the first one and no crossing is therefore allowed. For the irregular shape (d), the lack of any symmetry is responsible for the absence of crossings in the spectrum.

We discuss next the results in presence of a magnetic field B. Figure 4 compares the analytic and numeric results for a circular loop when $B = 0.5$ T. The magnetic field breaks the valley degeneracy of the loop eigenmodes, yielding asymmetric spectra with respect to energy inversion. We remark that figure 4 shows the results for a given valley. The results for the opposite valley, shown in appendix B, are shifted in the opposite direction restoring the symmetry of the spectrum for both energy and valley inversion ($\mathcal{C}$ symmetry). There is again a good qualitative agreement between QPM and Q2DM, the most noticeable

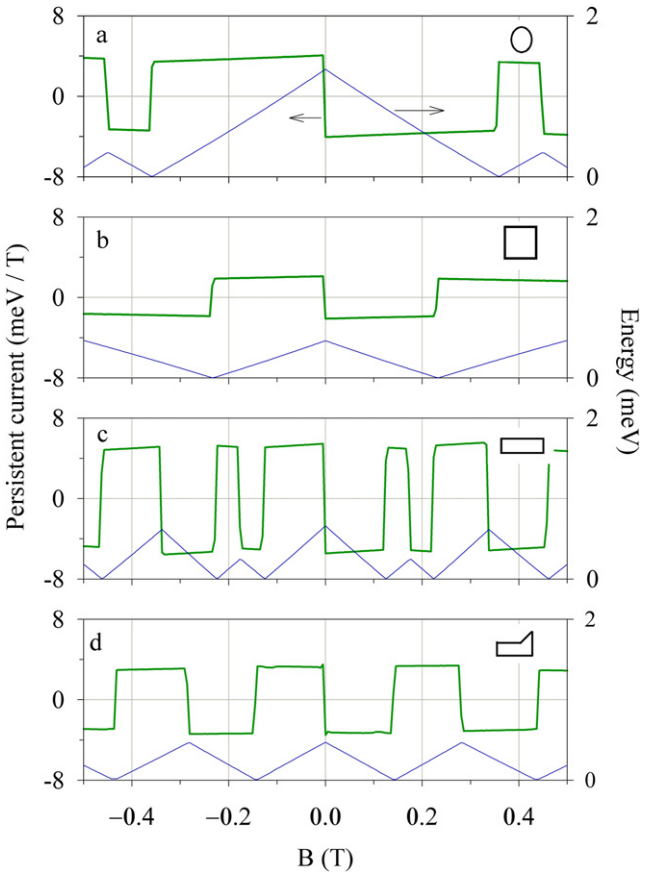

Figure 7. Persistent current J_1 (thick line, left scale) and energy E_1 (thin line, right scale) of the lowest positive state as a function of the magnetic field for a fixed perimeter loop and the different shapes indicated in each panel. Parameters as in figure 6.

difference being the denser bunching of the energy branches within Q2DM, as in the $B = 0$ cases discussed above.

In figure 5 we show the results of the 2D model at finite magnetic field for the different shapes. The field-induced asymmetry is similar when the geometrical structure changes. Branch anticrossings are present for nonsymmetric shapes, although they are not centered at zero energy but shifted vertically. Similarly to $B = 0$ (cf figure 3), we find that with an increase of the perimeter the shape-dependent features of the spectrum are washed out.

As a function of magnetic field, for a fixed loop dimension and shape, the loop spectrum shows a periodic behavior that is reminiscent of the Aharonov–Bohm effect. Figure 6 shows the result for a square in the QPM and Q2DM, both in good qualitative agreement. The energy branches come in doublets, originating from the two kink branches $f_{1,2}$ given by equation (1). The results in figure 6 are in general asymmetric with respect to energy inversion, in the same way as for the results as a function of perimeter (figure 5); the energy inversion symmetry being fulfilled at $B = 0$ only. For different shapes the results show a similar periodicity, only that the field spacings between branch doublets must be scaled by the enclosed flux Φ.

As with previous figures, the results of figure 6 are for a single valley; the energy branches for the reversed valley having the exactly opposite slope, as the chiral symmetry dictates. The magnetic field slope of the branches is clearly indicating that the loop sustains persistent currents in finite fields, as discussed already for trivial and topological circular rings in references [28] and [40], respectively. Hence, we investigate the shape dependence of the persistent current in topological loops as a possible probe of the geometric effects on topologically confined states. For definiteness, we focus on the current associated to the lowest positive-energy quasiparticle of the spectrum E_1 from the derivative

$$J_1 = \frac{\partial E_1}{\partial B}. \tag{8}$$

The persistent current J_1 for the different shapes is shown in figure 7 for a fixed perimeter of 500 nm. Due to the aforementioned valley and energy inversion symmetry, the persistent current has an odd symmetry with respect to field inversion, implying a vanishing value at zero field. The current is

characterized by a sequence of alternating plateaus of almost constant values. This is an effect of the nearly linear dispersion of the energy levels with magnetic field. Positive and negative plateaus correspond to persistent currents of opposite valleys, circulating with opposed chiralities. For very large perimeters the QPM predicts a B-dependence of the persistent current only through the flux Φ. Therefore, the shape dependence can be scaled by the loop surface. However, in smaller loops the Q2DM yields a nontrivial shape dependence. Along the sequence from high symmetry ((a), circle) to low symmetry ((b) square, c rectangle and d irregular shapes) the behavior looks qualitatively similar, but the plateau lengths are reduced due to the increased number of field transitions. This is also expected since the flux Φ is reduced for the deformed loops. Therefore, measuring the persistent current yields valuable information on the geometrical structure of the loop.

4. Conclusions

We have investigated the confined states in topological loops built in BLG. We have devised an analytical model, the QPM, based on the infinite straight kink, that provides the wavelength quantization along the loop perimeter. In addition, a full Q2DM, valid at low energies, has been numerically solved in order to ascertain the validity of the analytical model. A general good agreement between both models is found. For large sizes, the energy spectra are almost insensitive to the loop shape, as expected from QPM. For small sizes, we have found that Q2DM reflects shape dependence in the emergence of zero-energy crossings for circles, alternating crossings-anticrossings for squares, and only anticrossings for other more irregular structures. The magnetic field introduces energy-inversion asymmetries of the spectrum for a single valley and Aharonov–Bohm periodicities. Shape-dependent anticrossings in small loops are also present with magnetic fields. Finally, we have found that persistent currents are sensitive to shape-dependent features in presence of magnetic fields, which makes electric currents a useful tool to look into bound states in topological systems.

Overall, our results are helpful for tailoring potential structures, finding the optimal geometry for possible applications in quantum computation with topological qubits or for valleytronic devices. Since there could be deviations from the intended symmetry due to fabrication limitations, our study emphasizes the importance of taking into account emerging spatial asymmetries for a careful characterization of the underlying physical system.

Acknowledgments

We acknowledge support from Grant No. PID2020-117347GB-I00 funded by MCIN/AEI/10.13039/501100011033, MINECO/AEI/FEDER María de Maeztu Program for Units of Excellence MDM2017-0711, and GOIB Grant No. PDR2020-12.

Data availability statement

All data that support the findings of this study are included within the article (and any supplementary files).

Appendix A. Modeling

The Q2DM low energy Hamiltonian, equation (5), requires a specific spatial dependence of the asymmetric potential $V_a(x, y)$. This appendix contains the details of the modeling of different loop shapes with $V_a(x, y)$ smooth profiles parameterized with a diffusivity s. The circle is described by a simple combination of logistic functions in the radial coordinate $r = \sqrt{x^2 + y^2}$,

$$V_a^{(cir)}(r) = V_a^{(in)}\mathcal{F}(r; R_0, s) + V_a^{(out)}\left(1 - \mathcal{F}(r; R_0, s)\right), \tag{A1}$$

where $V_a^{(in,out)}$ are the constant values of asymmetric potential inside/outside of the loop and the logistic function reads

$$\mathcal{F}(r; R_0, s) = \frac{1}{1 + \exp[(r - R_0)/s]}. \tag{A2}$$

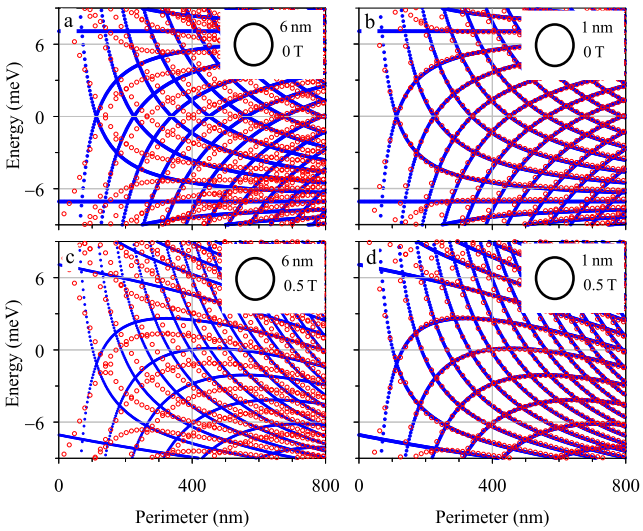

Figure 8. Energy eigenvalues of circular loops as a function of perimeter for different diffusivities and magnetic fields as indicated in each panel. Small symbols (blue) and open circles (red) correspond, respectively, to QPM and Q2DM. Notice that the analytic model exactly reproduces the low-energy numerical results only in the limit of sharp potentials (b) and (d).

To describe smooth square and rectangle shapes we first introduce the ranges of the Cartesian coordinates $x \in [x_a, x_b]$, $y \in [y_a, y_b]$ representing the loop inner area and then use a similar smooth parametrization in each Cartesian direction. Namely,

$$V_{\rm a}^{(\rm squ,rect)}(r) = V_{\rm a}^{(\rm in)}\mathcal{F}_{\rm 2D}(x,y) + V_{\rm a}^{(\rm out)}\left(1 - \mathcal{F}_{\rm 2D}(x,y)\right), \tag{A3}$$

where

$$\mathcal{F}_{\rm 2D}(x,y) = \left(\mathcal{F}(x;x_b,s) - \mathcal{F}(x;x_a,s)\right)\left(\mathcal{F}(y;y_b,s) - \mathcal{F}(y;y_a,s)\right). \tag{A4}$$

Finally, for the irregular shape we use the same modeling of equation (A3) but with the modification that y_b is no longer constant but the following piecewise function of x

$$y_b(x) = \begin{cases} 0, & x < 0, \\ xy_b/x_b, & x > 0. \end{cases} \tag{A5}$$

Notice that we assume centered positions of the loop, with $x_{a,b} = \mp L_x/2$ and $y_{a,b} = \mp L_y/2$. For completeness, the perimeters for the different shapes are $\mathcal{P}_{\rm cir} = 2\pi R_0$, $\mathcal{P}_{\rm squ} = 4L_x$, $\mathcal{P}_{\rm rect} = 2(L_x + L_y)$, $\mathcal{P}_{\rm irr} = \frac{3}{2}(L_x + L_y) + \frac{1}{2}\sqrt{L_x^2 + L_y^2}$.

The QPM analytic model of section 2.1 is based on the energies of a sharp straight kink [24]. Therefore, we expect an agreement between QPM and Q2DM in the limit of small values of s. Such comparison is explicitly made in figure 8 for circles with 6 and 1 nm diffusivities. Panels b and d of figure 8 indeed show the expected agreement for $s = 1$ nm and magnetic fields of 0 and 0.5 Teslas. On the other hand, the 6 nm results (figures 8(a) and (c)) show increasing deviations toward the low perimeter and large energy directions. We also stress here that the QPM-Q2DM precise correspondence of figures 8(b) and (d) confirms the absence of any Berry-phase deviation from integer n's in the quantization rule given by equation (4).

Appendix B. Valley reversal

To better illustrate the relation between the different valleys in presence of a magnetic field, figure 9 shows the opposite-valley results with respect to figure 4. Due to chiral symmetry $\mathcal{C}$ eigenstates of reversed valleys have exactly sign-reversed energies.

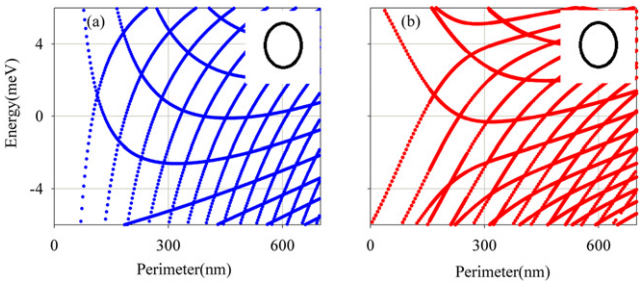

Figure 9. Same results of figure 4 but for the opposite valley.

ORCID iDs

David Sánchez https://orcid.org/0000-0002-2549-7071
Llorenç Serra https://orcid.org/0000-0001-8496-7873

References

[1] Landau L D and Lifshitz E M 1981 *QuantumMechanics (Non-Relativistic Theory)* (Oxford: Butterworth-Heinemann) p 29
[2] Bransden B H and Joachain C J 2006 *Physics of Atoms and Molecules* (Harlow: Pearson)
[3] Ihn T 2009 *Semiconductor Nanostructures: Quantum States and Electronic Transport* (Oxford: Oxford University Press)
[4] Trauzettel B, Bulaev D V, Loss D and Burkard G 2007 Spin qubits in graphene quantum dots *Nat. Phys.* **3** 192–6
[5] Pereira J M, Vasilopoulos P and Peeters F M 2007 Tunable quantum dots in bilayer graphene *Nano Lett.* **7** 946–9
[6] Recher P, Nilsson J, Burkard G and Trauzettel B 2009 Bound states and magnetic field induced valley splitting in gate-tunable graphene quantum dots *Phys. Rev.* B **79** 085407
[7] Zarenia M, Pereira J M, Peeters F M and Farias G A 2009 Electrostatically confined quantum rings in bilayer graphene *Nano Lett.* **9** 4088–92
[8] Recher P and Trauzettel B 2010 Quantum dots and spin qubits in graphene *Nanotechnology* **21** 302001
[9] González J W, Santos H, Pacheco M, Chico L and Brey L 2010 Electronic transport through bilayer graphene flakes *Phys. Rev.* B **81** 195406
[10] González J W, Santos H, Prada E, Brey L and Chico L 2011 Gate-controlled conductance through bilayer graphene ribbons *Phys. Rev.* B **83** 205402
[11] Orellana P A, Rosales L, Chico L and Pacheco M 2013 Spin-polarized electrons in bilayer graphene ribbons *J. Appl. Phys.* **113** 213710
[12] da Costa D R, Zarenia M, Chaves A, Farias G A and Peeters F M 2014 Analytical study of the energy levels in bilayer graphene quantum dots *Carbon* **78** 392–400
[13] Eich M *et al* 2018 Spin and valley states in gate-defined bilayer graphene quantum dots *Phys. Rev.* X **8** 031023
[14] Kurzmann A *et al* 2019 Charge detection in gate-defined bilayer graphene quantum dots *Nano Lett.* **19** 5216–21
[15] Clericò V *et al* 2019 Quantum nanoconstrictions fabricated by cryo-etching in encapsulated graphene *Sci. Rep.* **9** 13572
[16] Banszerus L *et al* 2020 Electron–hole crossover in gate-controlled bilayer graphene quantum dots *Nano Lett.* **20** 7709–15
[17] Banszerus L *et al* 2021 Pulsed-gate spectroscopy of single-electron spin states in bilayer graphene quantum dots *Phys. Rev.* B **103** L081404
[18] Min H, Hill J E, Sinitsyn N A, Sahu B R, Kleinman L and MacDonald A H 2006 Intrinsic and Rashba spin–orbit interactions in graphene sheets *Phys. Rev.* B **74** 165310
[19] Yao Y, Ye F, Qi X-L, Zhang S-C and Fang Z 2007 Spin–orbit gap of graphene: first-principles calculations *Phys. Rev.* B **75** 041401
[20] Gmitra M, Konschuh S, Ertler C, Ambrosch-Draxl C and Fabian J 2009 Band-structure topologies of graphene: spin–orbit coupling effects from first principles *Phys. Rev.* B **80** 235431
[21] Sui M *et al* 2015 Gate-tunable topological valley transport in bilayer graphene *Nat. Phys.* **11** 1027–31
[22] Overweg H *et al* 2018 Topologically nontrivial valley states in bilayer graphene quantum point contacts *Phys. Rev. Lett.* **121** 257702
[23] Kraft R, Krainov I V, Gall V, Dmitriev A P, Krupke R, Gornyi I V and Danneau R 2018 Valley subband splitting in bilayer graphene quantum point contacts *Phys. Rev. Lett.* **121** 257703
[24] Martin I, Blanter Y M and Morpurgo A F 2008 Topological confinement in bilayer graphene *Phys. Rev. Lett.* **100** 036804
[25] Kane C L and Mele E J 2005 Quantum spin Hall effect in graphene *Phys. Rev. Lett.* **95** 226801
[26] Bernevig B A, Hughes T L and Zhang S-C 2006 Quantum spin Hall effect and topological phase transition in HgTe quantum wells *Science* **314** 1757
[27] König M, Wiedmann S, Brüne C, Roth A, Buhmann H, Molenkamp L W, Qi X-L and Zhang S-C 2007 Quantum spin Hall insulator state in HgTe quantum wells *Science* **318** 766
[28] Xavier L J P, Pereira J M, Chaves A, Farias G A and Peeters F M 2010 Topological confinement in graphene bilayer quantum rings *Appl. Phys. Lett.* **96** 212108
[29] Park C-H and Marzari N 2011 Berry phase and pseudospin winding number in bilayer graphene *Phys. Rev.* B **84** 205440
[30] McCann E and Koshino M 2013 The electronic properties of bilayer graphene *Rep. Prog. Phys.* **76** 056503
[31] Rozhkov A V, Sboychakov A O, Rakhmanov A L and Nori F 2016 Electronic properties of graphene-based bilayer systems *Phys. Rep.* **648** 1–104
[32] Benchtaber N, Sánchez D and Serra L 2021 Scattering of topological kink–antikink states in bilayer graphene structures *Phys. Rev.* B **104** 155303

[33] Jing L, Wang K, McFaul K J, Zern Z, Ren Y, Watanabe K, Taniguchi T, Qiao Z and Zhu J 2016 Gate-controlled topological conducting channels in bilayer graphene *Nat. Nanotechnol.* **11** 1060–5
[34] Chen H, Zhou P, Liu J, Qiao J, Oezyilmaz B and Martin J 2020 Gate controlled valley polarizer in bilayer graphene *Nat. Commun.* **11** 1202
[35] Lehoucq R B, Sorensen D C and Yang C 1998 *ARPACK Users Guide: Solution of Large-Scale Eigenvalue Problems with Implicitly Restarted Arnoldi Methods* (Philadelphia, PA: SIAM)
[36] Susskind L 1977 Lattice fermions *Phys. Rev.* D **16** 3031–9
[37] Nielsen H B and Ninomiya M 1981 Absence of neutrinos on a lattice: (I). Proof by homotopy theory *Nucl. Phys.* B **185** 20–40
[38] Hernández A R and Lewenkopf C H 2012 Finite-difference method for transport of two-dimensional massless Dirac fermions in a ribbon geometry *Phys. Rev.* B **86** 155439
[39] Zarenia M, Pereira J M, Farias G A and Peeters F M 2011 Chiral states in bilayer graphene: magnetic field dependence and gap opening *Phys. Rev.* B **84** 125451
[40] Recher P, Trauzettel B, Rycerz A, Blanter Y M, Beenakker C W J and Morpurgo A F 2007 Aharonov–Bohm effect and broken valley degeneracy in graphene rings *Phys. Rev.* B **76** 235404